ISSFD 2024: Extremely low-altitude lunar station keeping using eccentricity vector control

Harry Holt[1], Jack Yarndley[1], Roberto Armellin[1], Martin Lara[2], Claudio Bombardelli[3], Robert Howie[4] and Phil Bland[4]
[1]Te Pūnaha Ātea - Space Institute, University of Auckland, Auckland, New Zealand
harry.holt@auckland.ac.nz
[2]Scientific Computation & Technical Innovation Center, Universidad de La Rioja, Logroño, Spain
[3]Space Dynamics Group, Universidad Politécnica de Madrid, Madrid, Spain
[4]Space Science and Technology Centre, Curtin University, Perth, Australia

***Abstract*—This paper presents a station-keeping strategy for extremely low-altitude lunar orbits (eLLOs) using eccentricity-vector control. The desired altitude range of 18 ± 9km poses considerable challenges due to the Moon's highly nonlinear gravity field, and is too low for potentially stable frozen orbits. To overcome these challenges, we propose a station-keeping strategy based on the predictable nature of the polar phase plot for eccentricity, e, and argument of periapsis, ω, typical of low lunar orbits. This enables the optimisation of e and ω to maximise the time before altitude violation. sequential convex programming (SCP) is used to optimise the manoeuvres to provide a guidance strategy that could be implemented on-board. The results improve significantly on circularisation strategies, both in terms of Δv and frequency of manoeuvres. This is a general strategy applicable to different altitude lunar orbits and constraints.**

I. Introduction

Designing long-duration lunar orbiter missions poses considerable challenges due to the Moon's highly nonlinear gravity field and the third-body perturbations induced by the Earth and Sun. The absence of a lunar atmosphere provides the opportunity to explore extremely low-altitude orbits that offer unique scientific prospects, including high-resolution imaging, magnetometry, and gravitational studies.

Maintaining these orbits becomes particularly intricate. Significant past efforts have been directed towards stable near-frozen Lunar orbits to maintain such orbits. Frozen orbits around the Moon have been studied by various researchers, including Konopliv et al. [1], Lara [2], Russell and Lara et al. [3], and Folta and Quinn [4], amongst others. Most studies necessitate a simplification of the gravitational model, often to solely zonal terms. In addition, the altitudes considered rarely go below 50 km and show a lack of frozen orbits with low eccentricity close to polar latitudes [2]. Beckman and Lamb [5] studied the station-keeping prospects for the Lunar Reconnaissance Orbiter (LRO), which was designed to maintain an orbit of 50 ± 20 km. Singh et al. [6] have investigated the feasibility of quasi-frozen, near-polar and extremely low-altitude lunar orbits. However, their analysis currently allows for a large increase in eccentricity over time.

This work has been inspired by the Binar Prospector mission [7, 8, 9]. Binar's mission aims to achieve a extremely low-altitude lunar orbit (eLLO) with a range of altitudes around 18 ± 9 km, whilst maintaining a polar inclination. The conventional use of frozen orbits has proven inadequate for this mission's specific requirements, primarily due to its inclination, circular nature and low altitude. To overcome these challenges, we propose an alternative approach based on the predictable nature of the polar phase plot for eccentricity, e, and argument of periapsis, ω, typical of low lunar orbits [5]. This pattern exhibits almost repetitive nature for low eccentricities. As such, we can approximate the evolution of the $e - \omega$ profile - a feature that was named the "translation theorem" in [5].

A station-keeping strategy is developed based on the key insight of optimising the starting conditions in (e,ω) to maximise the time duration before the 18 ± 9 km altitude constraints are violated, a process which is facilitated by the "translation theorem". Upon violation, a new target (e,ω) pair is computed. The manoeuvre optimisation in done using sequential convex programming (SCP), and results are presented for different initial conditions with varying objectives such as minimising the number of manoeuvres and minimising the predicated total Δv.

The paper is structured as follows. Firstly, the Moon's dynamics are introduced, and a detailed analysis of the "translation theorem" is given in Section III-A. Next, the $e - \omega$ optimisation strategy is presented, and then a grid search over possible initial conditions is given in Section III-C. The SCP approach is discussed in Section III-D and the results presented in Section IV.

II. Problem Setup

A. Binar Prospector

Binar Prospector is an Australian lunar resource prospecting mission. The principal payload will be a magnetometer designed to identify localised accessible volatile deposits and mineralisation. It will have a novel mission architecture, with a propulsion systems and fuel payload dedicated to maintaining eLLOs. Prospecting for such resources requires high-resolution geophysical datasets, of which magnetometry is a prerequisite. A high-resolution magnetic survey would provide a deeper understanding of the geology of the Moon, and its resource potential, but the current global lunar magnetic survey has insufficient resolution to deliver that. In magnetometry, because the field decays with the inverse of distance, better resolution means lower altitude observations. However, such eLLOs require regular station-keeping manoeuvres and often a prohibitively high Δv budget, shortening the mission lifetime and making them undesirable for large missions with multiple payloads.

By being the first lunar mission with magnetometers as the primary payload, Binar Prospector will be able to prioritise

extremely low altitude data collection. As such, the nominal goal is to orbit within a range of altitudes around 18 ± 9 km at polar inclinations for a mission duration of 3 months. This architecture should deliver a 10 fold improvement on the current average magnetic survey resolution, and it will explore the potential of a radically new mission architecture. Low altitude is a requirement for high resolution magnetometry, but by exploring the ability to inexpensively acquire high value, high resolution datasets at low altitudes, it could open up a range of other mission types and profiles.

B. Dynamical Model

When considering eLLOs, the main disturbances to account for are the highly non-spherical gravity field of the Moon and the gravitational pull of the Earth. In this work, given the low altitude of 18 ± 9 km, we are going to focus our analysis on the non-spherical gravity field of the Moon. The gravitational field is thus given by the potential:

$$V = -\frac{\mu}{r} - R_m, \tag{1}$$

where μ is the gravitational parameter of the central body, r the distance of the satellite to the origin, and R_m is the disturbing potential due to the non-centrality of the central body's gravitational potential:

$$R_m = \frac{\mu}{r} \sum_{j\geq 2} \frac{\alpha^j}{r^j} \sum_{k=0}^{j} \left(C_{j,k} \cos k\lambda + S_{j,k} \sin k\lambda\right) P_{j,k}(\sin \varphi) \tag{2}$$

where α is the equatorial radius of the central body, φ is latitude, λ is longitude, $C_{j,k}$ and $S_{j,k}$ are harmonic coefficients, and $P_{i,j}$ are associated Legendre polynomials of degree i order j. Data for the harmonic coefficients, and thus the lunar gravity field, was obtained using the GRAIL mission data from the Jet Propulsion Laboratory (specifically the GRGM1200A model[1], truncated to 660). The body-fixed frame, where these spherical harmonics are defined, is the Lunar principal axis (PA) frame[2]. The orbital propagation is done in the Lunar Mean Equator of Date J2000 (LME2000), defined as: $+z$ axis points toward Moon's north polar of data J2000, $+x$ axis points toward the intersection between the Moon's equator of date and the J2000 equator; $+y$ axis completes the right-hand frame. The origin of this frame is Moon's centre of mass.

III. Methodology

A. Dynamical analysis and the Translation "Theorem"

A popular reformulation of (1) in the usual Keplerian elements $(a, e, I, \Omega, \omega, M)$ was provided by Kaula [10]. We rewrite the disturbing part of it in closed form of the eccentricity as [11]

$$\mathcal{P} \equiv -R_m = -\frac{\mu}{a}\left(\frac{a^2\eta}{r^2}\right) \sum_{i\geq 2} \sum_{j=0}^{i} V_{i,j}, \tag{3}$$

[1]https://pgda.gsfc.nasa.gov/products/50
[2]moon_pa_de421_1900-2050.bpc

in which

$$V_{i,j} = \frac{\alpha^i}{p^i}\eta \sum_{k=0}^{i} F_{i,j,k} \sum_{m=0}^{i-1} \binom{i-1}{m} \frac{e^m}{2^m} \sum_{l=0}^{m} \binom{m}{l} \big[(S_{i,j}\cos\psi_{i,j,k} - C_{i,j}\sin\psi_{i,j,k})\sin(i-2k-m+2l)f + (\cos\psi_{i,j,k} \times C_{i,j} + S_{i,j}\sin\psi_{i,j,k})\cos(i-2k-m+2l)f\big], \tag{4}$$

where $F_{i,j,k} \equiv F_{i,j,k}(I)$ denote Kaula's inclination functions,

$$\psi_{i,j,k} = (i-2k)\omega + j\phi - (i-j)_\pi, \tag{5}$$

and $\#_\pi = \frac{\pi}{2}(\#\bmod 2)$ denotes a parity correction. $p = a\eta^2$, $\eta = \sqrt{1-e^2}$, $\phi = \Omega - \dot{\vartheta}t$ is the argument of the node in the moon's fixed frame, with t denoting the time and $\dot{\vartheta}$ the moon's rotation rate, and $f \equiv f(M, e)$ is true anomaly. The problem is conservative in the moon-fixed frame. Hence the scalar function $\mathcal{H} = -\frac{1}{2}(\mu/a) - \dot{\vartheta}H + \mathcal{P}$ (the Hamiltonian) remains constant, where $H = \Theta\cos I$ denotes the projection of the angular momentum vector along the moon's rotation axis, and $\Theta = \sqrt{\mu a}\eta$ is the specific angular momentum.

Kaula's formulation discloses the different time scales of the problem. The short-period terms, related to M, simply modulate the long-term dynamics driven by the slow motion of ω. Deep tesseral resonances between the variation of ϕ and the mean motion $n = \sqrt{\mu/a^3}$ may have dominant long-period effects. But they are not a concern for low-lunar orbits, whose periods barely reach 2 hours compared to the month spent by the moon on its rotation. Still, ϕ evolves much faster than ω, which typically completes one period in a scale of years. [5]

While the moon's harmonic coefficients are $\mathcal{O}(10^{-4})$ or smaller, the Coriolis term $-\dot{\vartheta}H = -(\dot{\vartheta}/n)(\mu/a)\eta\cos I$ is $\mathcal{O}(10^{-3})$ compared to the Keplerian $-\frac{1}{2}(\mu/a)$ for low-lunar orbits. This fact makes the computation of perturbation solutions natural, whose use is customary in the preliminary steps of mission design. In particular, a transformation from mean to osculating elements is used to remove the short-period terms from (3) up to higher-order effects, thus reducing the dimension of the problem from 3 to 2 degrees of freedom. This transformation turns the Hamiltonian into $\mathcal{H}' = -\frac{1}{2}(\mu/a') - \dot{\vartheta}H' + \langle\mathcal{P}\rangle_M$, where primes denote mean elements or functions of them. From (3)

$$\langle\mathcal{P}\rangle_M = \left\langle \mathcal{P}\frac{r^2}{a^2\eta}\right\rangle_f = -\frac{\mu}{a'}\sum_{i\geq 2}\langle V_{i,0}\rangle_f - \frac{\mu}{a'}\sum_{i\geq 2}\sum_{j=1}^{i}\langle V_{i,j}\rangle_f. \tag{6}$$

Making $l = k + \frac{1}{2}(m-i)$ in (4), we obtain

$$\langle V_{i,j}\rangle_f = \frac{\alpha^i}{a'^i}\sum_{k=1}^{i} F'_{i,j,k}G_{i,k}(C_{i,j}\cos\psi'_{i,j,k} + S_{i,j}\sin\psi'_{i,j,k}), \tag{7}$$

where $G_{i,k}$ are particular instances of Kaula's eccentricity functions $G_{i,k,l}$. In the fashion of Kaula's linear theory, an approximate solution is then obtained by combining the solution to the mean variations stemming from (6) with the short-period corrections in (3.76) of [10].

Terms of (6) with $j \geq 1$ depend on ϕ, whose period is brief compared to the time needed by the periselene of non-impact lunar orbits to repeat its path. Therefore, we remove these terms by an additional transformation to

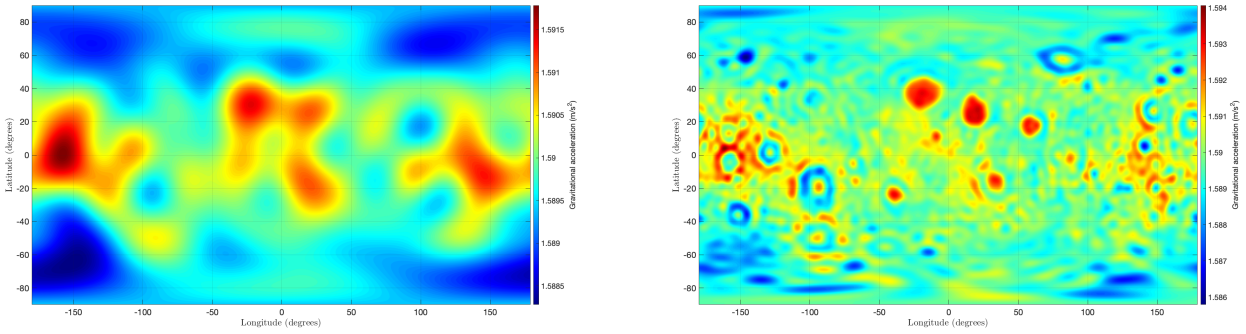

(a) SH: 9x9 Altitude 18 km

(b) SH: 51x51 Altitude 18 km

Fig. 1: Gravitational acceleration for 9x9 and 51x51 gravitational potentials at 18 km above the equatorial radius of the Moon, $\alpha = 1737.4$ km.

double-prime variables that makes $\langle\langle V_{i,j}\rangle_f\rangle_h = \langle V_{i,0}\rangle_f \equiv C_{i,0}(\alpha/a')^i \sum_{k=1}^{i} F'_{i,0,k} G_{i,k} \cos[(i-2k)\omega' - i_\pi]$, which is obtained making $j = 0$ in (6). These zonal terms only depend on ω and hence drive the long-term dynamics.

The solution in mean elements is analogously obtained using Kaula's approach. That is, the solution of the variations stemming from the perturbation $\langle\langle \mathcal{P}\rangle_M\rangle_h$ is complemented with similar periodic corrections to Kaula's (3.76). For instance, for the eccentricity $e'(t) = e''(t) + \sum_{i\geq 2}\sum_{j=1}^{i}\sum_{k=1}^{i} \Delta e'_{i,j,k}$, where, neglecting terms $\mathcal{O}(\dot\omega/\dot\vartheta)$ and $\mathcal{O}(\dot\Omega/\dot\vartheta)$,

$$\Delta e'_{i,j,k} = \frac{n'}{\dot\vartheta}\frac{2k-i}{j}\frac{\alpha^i}{a'^i}F'_{i,j,k}\frac{\eta'}{e'}G'_{i,k} \times (C_{i,j}\cos\psi'_{i,j,k} + S_{i,j}\sin\psi'_{i,j,k}) \qquad (8)$$

The term $n'/\dot\vartheta$ in (8) may reach two orders of magnitude for of low lunar orbits, thus showing the notably larger amplitude of these terms compared to the short-period corrections.

The double-averaging process turned both a and H into integrals. Moreover, the disturbing potential $\mathcal{P}'' = \mathcal{P}(a'', e'', i'', -, \omega'', -)$ is also an integral as follows from the constancy of $\mathcal{H}$. Therefore, for each point on the parameters plane (a'', H''), the long-term dynamics is described by a one-degree-of-freedom problem in the mean eccentricity and mean argument of the periapsis. In particular,

$$\frac{\mathrm{d}\omega''}{\mathrm{d}t} = \frac{\partial\mathcal{P}''}{\partial\Theta''}, \qquad \frac{\mathrm{d}e''}{\mathrm{d}t} = -\frac{\partial e''}{\partial\Theta''}\frac{\partial\mathcal{P}''}{\partial\omega''}. \qquad (9)$$

The equilibria of (9) yield orbits with constant eccentricity and frozen argument of the periapsis, on average—the so-called frozen orbits. The mean variation of the eccentricity vanishes for orbits with $\omega'' = \pm\frac{1}{2}\pi$, leaving a single condition for the vanishing of the mean variation of ω. Namely, $\Phi(e'', i'', \omega'' = \pm\frac{\pi}{2}; a'') = 0$, which can be viewed as the curve of frozen orbits $e'' = e''(i''; \omega'' = \pm\frac{\pi}{2}; a'')$.

Fig. 2 shows an example for $a = \alpha + 20$ km above the lunar surface. The mean selenopotential is truncated to degree 30, which is enough to illustrate the complexity of the frozen orbits problem. As shown in the left plot of Fig. (2), frozen lunar orbits exist for all inclinations. Yet, low-lunar frozen orbits only exist in very narrow strips about $I \approx 70$, 74, 78, and 86 deg, as shown in the right plot, where the dotted lines mark the eccentricity limit for impact.

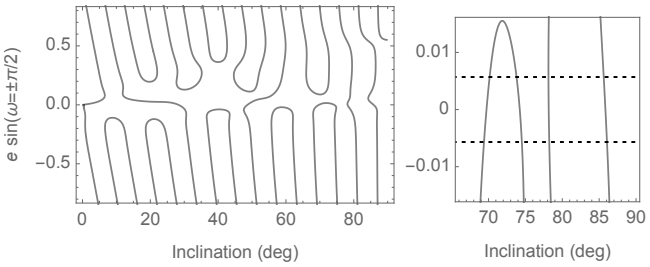

Fig. 2: Diagram of frozen orbits with a detail for high I.

On the other hand, the phase space of the integrable, reduced flow is made of fixed points, either of the elliptic or hyperbolic types, and closed curves. The fixed points correspond to frozen orbits. Apart from them, specific orbits will have oscillating or rotating periapses in the different regions of phase space bounded by the manifolds with the same Hamiltonian value of the hyperbolic fixed points, which may define either homoclinic or heteroclinic connections in phase space.

Contour plots of $\mathcal{P}'' = \mathcal{P}(e'', \omega''; a'', H'')$ show the reduced $(e''\omega'')$ phase space without need of integrating (9). A sequence a)–g) for increasing $I_{\text{circular}} = \arccos(H''/\sqrt{\mu a''})$ from $78° - 83°$ is depicted in Fig. 3. The dotted circle bounds the region of nonimpact orbits and h) shows a magnification of g). There are no frozen orbits in a), which is close to a saddle-node bifurcation. The bifurcation at $\omega = +\frac{\pi}{2}$ already occurred in b), where stable ($e = 0.015$) and unstable ($e = 0$) frozen orbits exist. However, increasing I_{circular} has the effect of increasing sharply the eccentricity of the frozen orbits, as shown in c), thus flattening the phase space in the non-impact region, as depicted in d). Eventually, the mean dynamics will be driven by almost horizontal lines, as illustrated in e) and f). Note that $\cos I = \eta^{-1}\cos I_{\text{circular}} \approx (1 + \frac{1}{2}e^2)\cos I_{\text{circular}}$, and hence I slightly decreases for increasing e.

Note that the amplitude of the periodic corrections due to tesseral and sectoral terms, previously illustrated with (8), could push the eccentricity vector clearly out of the allowed

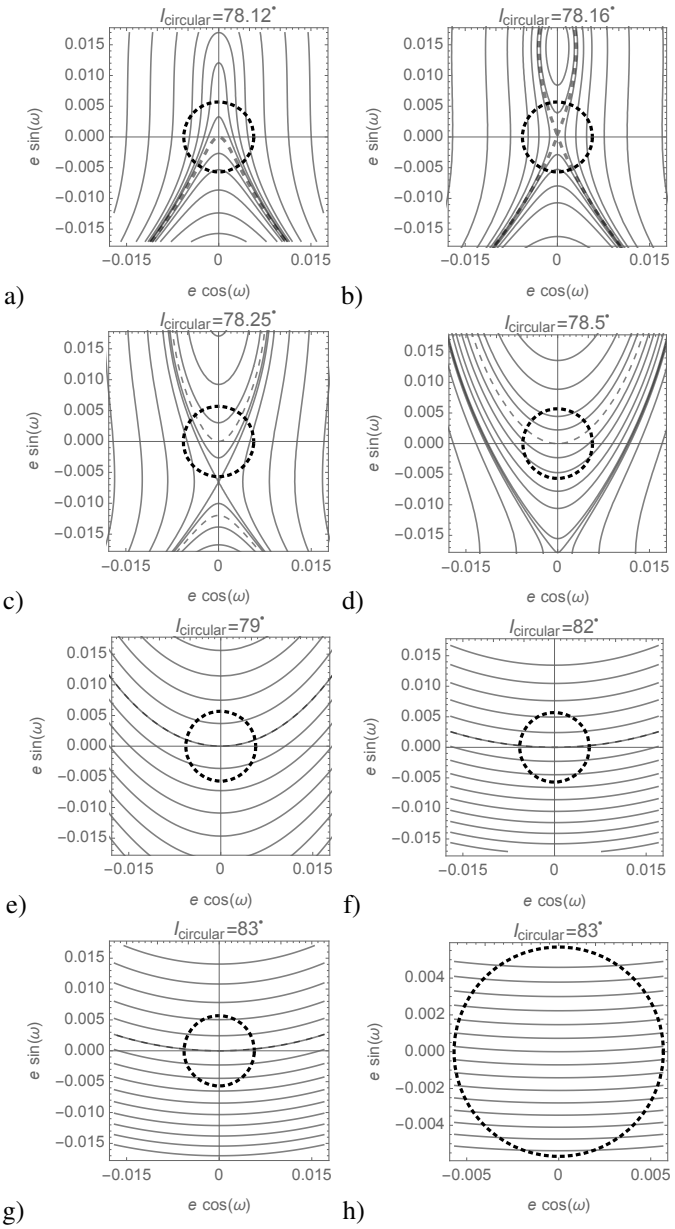

Fig. 3: Changes of the e-ω phase space with inclination.

region. Hence, for mission designing purposes, these important variations of the mean values must be superimposed to the long-term dynamics. That is, periodic corrections $\Delta(e\cos\omega)$ and $\Delta(e\sin\omega)$ must be computed analogously to (8) to be superimposed to the eccentricity vector plots. It is readily found that the dominant terms of these corrections are $\mathcal{O}(e^0)$ and do not depend on the argument of the periselene. For instance, for the contribution of the Moon's $C_{3,1} \approx 3\times10^{-5}$, straightforward computations yield

$$\Delta(e\cos\omega) = \frac{n}{\dot{\vartheta}} C_{3,1} \frac{\alpha^3}{a^3}\frac{3}{8}\cos I\left(11-15\cos^2 I\right)\cos\phi + \mathcal{O}(e),$$
$$\Delta(e\sin\omega) = -\frac{n}{\dot{\vartheta}} C_{3,1} \frac{\alpha^3}{a^3}\frac{3}{8}\left(1-5\cos^2 I\right)\sin\phi + \mathcal{O}(e).$$

Therefore, up to $\mathcal{O}(e)$, the monthly pattern generated by the eccentricity vector when starting from the same a, I, and ϕ, is

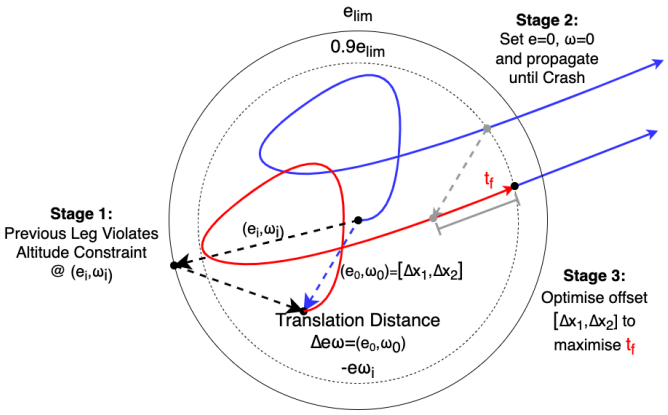

Fig. 4: Diagram illustrating the $e-\omega$ optimisation. $\Delta e\omega$ indicates the translation distance, which is balanced against the objective of maximising t_f.

the same irrespective of the initial e and ω values—a feature that was named the "translation theorem" in [5].

B. Optimising $e-\omega$ translation

For a given initial condition, i,ϕ pair, we can nominally set $e_0 = 0, \omega_0 = 0$ and propagate the natural evolution of the orbit until it crashes into the lunar surface. Approximating this evolution as the true evolution, the "translation theorem" mentioned above, it is possible to optimise the initial off-set in (e_0,ω_0) to maximise the time duration before $e \geq e_{lim}$. Here where e_{lim} is given by the 18 ± 9 km altitude constraints.

Fig. 4 illustrates this $e-w$ optimisation scheme, which is also discussed in Algorithm 1. Figures 5 show the natural motion of of an orbit from a given initial condition, with $a = 1755.4$km, $i = 86°$ in 9×9 and 51×51 spherical harmonics. The evolution at (e,ω)=$(0,0)$ is generated in blue. This is then "translated" to maximise the duration with $e < e_{lim}$ by finding the initial offset (e_0,ω_0), shown in orange. The true propagation at (e_0,ω_0) is show in yellow. This strategy is discussed in Algorithm 1, where the objective is set to *Time* by setting $\lambda = 0$.

Using the newly obtained (e_0,ω_0), the spacecraft needs to perform a manoeuvre to go from (e_i,ω_i) to this desired (e_0,ω_0). Subsequently, the spacecraft can be propagated in the natural dynamics until $e \geq e_{lim}$. Upon this violation, the whole process can be repeated as the spacecraft is effectively in a new set of "initial conditions".

C. Station-Keeping Strategy

Using the $e-\omega$ translation strategy discussed above, there are two remaining variables for the mission designer to consider when defining the SK strategy.

- First: determine the weighting of the Objective function. $\lambda = 0$ corresponds to $J = t_f$. This aims to maximise the duration of natural motion for the next SK segment. Its a greedy approach to allow a long period before the next SK manoeuvre is required. Alternatively, if $\lambda \neq 0$, then the objective begins to balance the time-of-flight with the

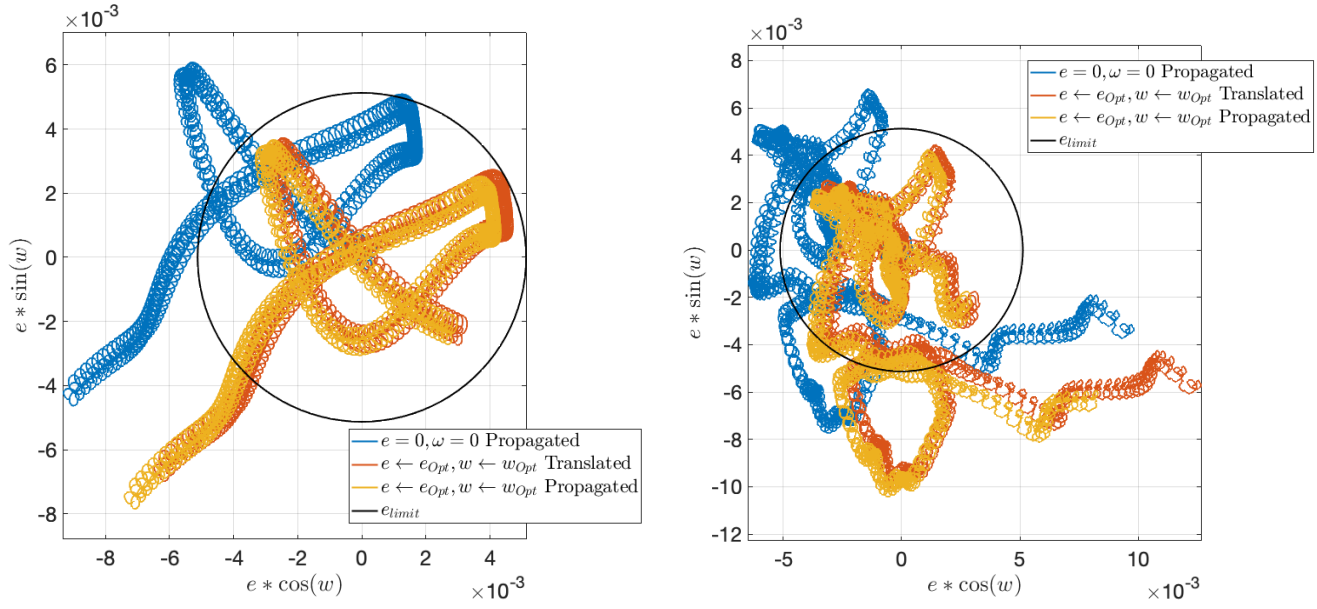

(a) SH: 9x9 (b) SH: 51x51

Fig. 5: Natural Motion of a spacecraft with $a = 1755.4$km, $i = 86°$ in 9×9 and 51×51 spherical harmonics. The evolution at $e = 0, \omega = 0$ is generated in blue. This is then "translated" to maximize the duration with $e < e_{lim}$ by finding the initial offset (e_0, ω_0), shown in orange. The true propagation at (e_0, ω_0) is show in yellow.

Algorithm 1 $e - \omega$ optimisation

Extract current time t and state $a, e, i, \Omega, \omega, \theta$ ▷ Violate SK requirements
Store $e_i = e$, $\omega_i = \omega$ ▷ Initial location for Translation Manoeuvre
Set $e = 0$, $\omega = 0$ ▷ Re-centre for $e - \omega$ optimisation
while $|r| > R_{\text{Moon}}$ **do** ▷ Natural Motion until it crashes into Moon Radius
    Propagate Ballistic Trajectory
Store $e(t)$ and $\omega(t)$ ▷ Evolution of e and ω
Set eccentricity limit e_{lim} ▷ Defined by the altitude requirements
Let the optimisation vector be $\Delta x_1 = e_0 \cos(\omega_0)$ and $\Delta x_2 = e_0 \sin(\omega_0)$ ▷ Initial off-set that is to be optimised
Define Translation Distance $\Delta e\omega = \sqrt{(\Delta x_1 - e_i \cos(\omega_i))^2 + (\Delta x_2 - e_i \sin(\omega_i))^2}$ ▷ Distance from e_i, ω_i to the newly optimised e_0,ω_0
Set the Objective, $J(\lambda) = \frac{t_f}{\Delta e\omega^\lambda}$ ▷ Use $\lambda = 0$ to maximise time, $\lambda = 1$ for a trade-off
Optimise Δx_1 and Δx_1 to maximise $J(\lambda)$ such that $\sqrt{(\Delta x_1 + e(t)\cos(\omega(t)))^2 + (\Delta x_2 + e(t)\sin(\omega(t)))^2} < e_{lim}\ \forall\, t \leq t_f$ ▷ Maximise $J(\lambda)$ for states inside e_{lim}
Compute $e_0 = \sqrt{\Delta(e\cos\omega)^2 + \Delta(e\sin\omega)^2}$ and $\omega_0 = \arctan(\Delta(e\sin\omega)/\Delta(e\cos\omega))$ ▷ Optimal initial conditions

"translation" distance, which acts as a proxy for the Δv required for SK manoeuvre from (e_i, ω_i) to (e_0, ω_0).

- Secondly, determine a suitable set of initial conditions i_0, ϕ_0 that helps reduce the SK cost. This can either be maximising the time interval between station-keeping manoeuvres, or reducing the total Δv cost.

In this work, the initial conditions are sought by setting $\lambda = 0$, and therefore optimising for the *time* between manoeuvres. A grid search on both i_0, ϕ_0 was performed, with $1°$ spacing in inclination, and $10°$ spacing in ϕ_0. In this initial grid search, the manoeuvres themselves are assumed to be possible and instantaneous. The total number of manoeuvres (assuming a bi-impulsive transfer) and the translation distance $\Delta e\omega$ are stored for each initial condition. The results for 9×9 spherical harmonics are shown in Fig. 6. Using this, three initial conditions appear promising: the minimum number of manoeuvres is 26 for $i_0 = 94°$, $\phi_0 = 127.76°$ and $i_0 = 86°$, $\phi_0 = 357.76°$; the minimum translation distance occurs at $i_0 = 94°$, $\phi_0 = 177.76°$; and the minimum average distance is at $i_0 = 94°$, $\phi_0 = 157.76°$. The same analysis was also run for 51×51 spherical harmonics, with a grid spacing of $5°$ in ϕ_0, to see if the pattern remains viable or not - see Fig. 7. The minimum number of manoeuvres minimum number of manoeuvres is 24 for $i_0 = 88°$, $\phi_0 = 342.76°$; the minimum translation distance occurs at $i_0 = 87°$, $\phi_0 = 7.76°$; and the minimum average distance is also at $i_0 = 87°$, $\phi_0 = 7.76°$.

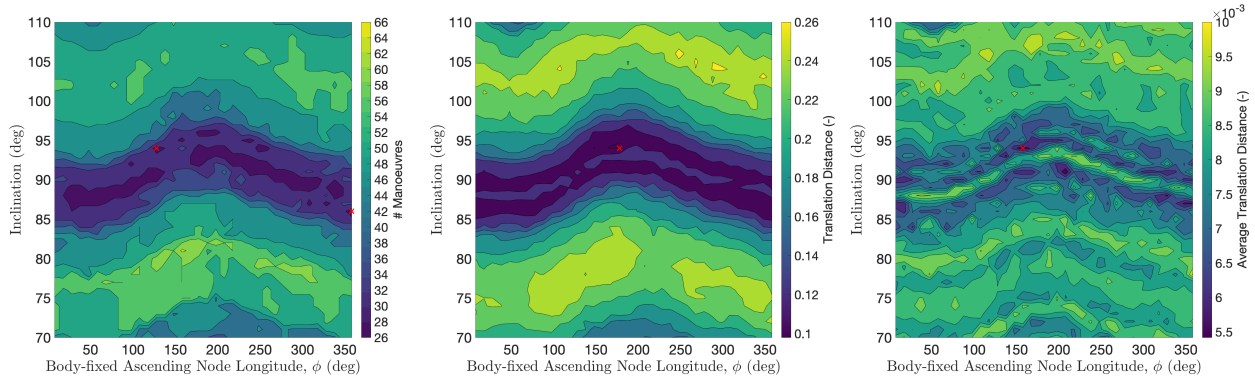

(a) Number of Manoeuvres (b) Total Translation Distance (c) Average Translation per Manoeuvre

Fig. 6: Grid Search for i_0, ϕ_0 in 9×9 Spherical Harmonics. The minimum number of manoeuvres is 26 for $i_0 = 94°$, $\phi_0 = 127.76°$ and $i_0 = 86°$, $\phi_0 = 357.76°$, whilst the minimum translation distance occurs at $i_0 = 94°$, $\phi_0 = 177.76°$, with the minimum average distance at $i_0 = 94°$, $\phi_0 = 157.76°$.

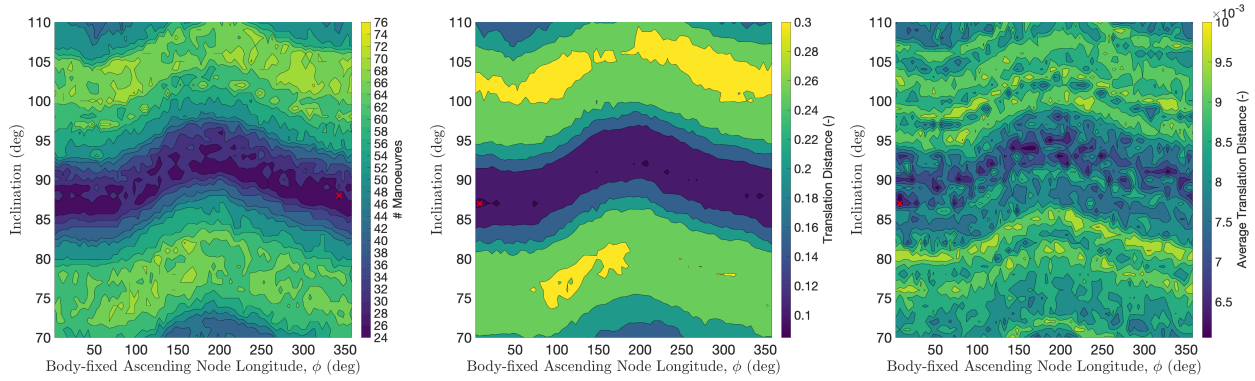

(a) Number of Manoeuvres (b) Total Translation Distance (c) Average Translation per Manoeuvre

Fig. 7: Grid Search for i_0, ϕ_0 in 51×51 Spherical Harmonics. The minimum number of manoeuvres is 24 for $i_0 = 88°$, $\phi_0 = 342.76°$, whilst the minimum translation distance occurs at $i_0 = 87°$, $\phi_0 = 7.76°$, with the minimum average distance also at $i_0 = 87°$, $\phi_0 = 7.76°$.

D. Convex Optimisation

Initially, the manoeuvre optimisation involved approximating manoeuvres with Lambert transfers and subsequently refining trajectory adjustments using MATLAB's fsolve. However, for a more accurate assessment of the Δv required, a more sophisticated approach using convex optimisation techniques was implemented. Applying the general approach of SCP [12], we start by finding an appropriate linearisation of the dynamical system. The dynamics of the spacecraft are provided with the state $\mathbf{x} = [\mathbf{r}, \mathbf{v}]$:

$$\dot{\mathbf{x}} = f(\mathbf{x}, \mathbf{\Delta v}, t) = \begin{cases} \dot{\mathbf{r}} = \mathbf{v} \\ \dot{\mathbf{v}} = \nabla V + \delta(t - t_n)\mathbf{\Delta v} \end{cases} \tag{10}$$

where μ is the gravitational constant of the Moon, m the mass, and $0 \leq T \leq 1$ the thrust of the spacecraft, which is normalized to $T_{\max}$.

A ballistic arc is used as the reference trajectory for linearization. This was often close to the optimal low-thrust trajectory due to the relatively short time-frames experienced when compared to some low-thrust applications. Thus, given a reference trajectory $(\bar{\mathbf{x}})$, the dynamical linearization can be performed, which is calculated along segments of the reference trajectory, where each discretisation segment is 10 minutes. An impulsive model is used here, but a zero-order-hold (ZOH) control model could easily be considered in future work. Thus, we obtain the discrete form of the dynamics for $n = 1, 2, ..., N$, which is able to be used as a convex constraint:

$$\mathbf{x}_{n+1} = A_n \mathbf{x}_n + B_n \mathbf{\Delta v}_n + C_n \tag{11}$$

with

$$A_n = \left[\frac{\partial}{\partial \mathbf{x}} \int_{t_n}^{t_{n+1}} \dot{\mathbf{x}} \, \mathrm{d}t \right] \Bigg|_{(\bar{\mathbf{x}}_n, \mathbf{\Delta}\bar{\mathbf{v}}_n)} \tag{12}$$

$$B_n = \left[\frac{\partial}{\partial \mathbf{\Delta v}} \int_{t_n}^{t_{n+1}} \dot{\mathbf{x}} \, \mathrm{d}t \right] \Bigg|_{(\bar{\mathbf{x}}_n, \mathbf{\Delta}\bar{\mathbf{v}}_n)} \tag{13}$$

$$C_n = \bar{\mathbf{x}}_n - A_n \bar{\mathbf{x}}_\mathbf{n} - B_n \mathbf{\Delta v}_n \tag{14}$$

The matrix A_n is the state transition matrix (STM) and is computed via automatic differentiation (AD). The process to use AD is as follows: the dynamical equations are placed into an adaptive step-size numerical integrator, and AD is used

to calculate the Jacobian of the output with respect to the input state and control. The Vern9 [13] numerical integrator was used from `DifferentialEquations.jl` [14] with absolute tolerance 10^{-12} and relative tolerance 10^{-12}, and `ForwardDiff.jl` [15] was used to perform the forward-mode automatic differentiation. The dynamics are left in their Cartesian form. The controllable parameter is the Δv added to the velocity at each node.

Additionally, we can perform a linearization on the altitude constraints by introducing an additional variable for each segment, $\mathbf{h}_n = [h_n^{\text{min}}, h_n^{\text{max}}]$. This is a 2-dimensional vector containing the minimum and maximum height encountered in segment n. The linearized constraint for $\mathbf{h}_n$ is therefore:

$$\mathbf{h}_{n+1} = D_n \mathbf{x}_n + E_n \boldsymbol{\Delta}\mathbf{v}_n + F_n \tag{15}$$

with

$$D_n = \left[\frac{\partial}{\partial \mathbf{x}} h^* \left(\int_{t_n}^{t_{n+1}} \dot{\mathbf{x}}\, \mathrm{d}t\right)\right]\Bigg|_{(\bar{\mathbf{x}}_n, \boldsymbol{\Delta}\bar{\mathbf{v}}_n)} \tag{16}$$

$$E_n = \left[\frac{\partial}{\partial \boldsymbol{\Delta}\mathbf{v}} h^* \left(\int_{t_n}^{t_{n+1}} \dot{\mathbf{x}}\, \mathrm{d}t\right)\right]\Bigg|_{(\bar{\mathbf{x}}_n, \boldsymbol{\Delta}\bar{\mathbf{v}}_n)} \tag{17}$$

$$F_n = \bar{\mathbf{h}}_n - D_n \bar{\mathbf{x}}_\mathbf{n} - E_n \boldsymbol{\Delta}\mathbf{v}_n \tag{18}$$

where the function h^* takes the integration as input and returns $\mathbf{h}$, and $\bar{\mathbf{h}}$ is derived from the reference trajectory. All of these matrices are calculated using AD in a similar manner to A_n. The altitude constraint is therefore:

$$\begin{aligned} h_n^{\text{min}} &\geq \mathrm{a}^{\text{min}} \\ h_n^{\text{max}} &\leq \mathrm{a}^{\text{max}} \end{aligned} \tag{19}$$

with a_{min} and a_{max} the minimum and maximum permitted altitudes respectively.

Because the optimization problem is formulated using Cartesian orbital elements, we must also use linearization for the terminal target constraint, wherein we target a specific eccentricity e, argument of periapsis ω, and semi-major axis a. This target is denoted $y_{\text{target}} = [e, \omega, a]$. The semi-major axis is targeted to correct for the drift that may occur if we only optimally target e and ω. The linearized terminal constraint is thus:

$$G\mathbf{x}_N + H = y_{\text{target}} \tag{20}$$

with

$$G = \left.\frac{\partial \mathbf{c}}{\partial \mathbf{x}}\right|_{(\bar{\mathbf{x}}_N)} \tag{21}$$

$$H = \bar{y}_{\text{target}} - G\bar{\mathbf{x}}_N \tag{22}$$

where $\mathbf{c}$ is a function which obtains the classical orbital elements $y = [e, \omega, a]$ from the Cartesian state, and $\bar{y}_{\text{target}}$ derived from the reference trajectory. The initial state constraint is:

$$\mathbf{x}_1 = \mathbf{x}_{\text{initial}} \tag{23}$$

The objective function is to minimize the Δv use throughout the trajectory. This form of objective necessitates obtaining the 2-norm of the control, which can be achieved through a lossless relaxation via a second-order-cone (SOC) constraint:

$$\Delta v_n \geq ||\Delta \mathbf{v}_n||_2 \quad \text{(SOC)} \tag{24}$$

with the 2-norm denoted by the non-bold Δv_n. Because we are minimizing Δv_n, this constraint is binding at optimality.

Combined, these constraints define a convex optimization problem, but this generally exhibits significant convergence and feasibility challenges. A common approach to resolving these issues is the introduction of trust regions and virtual controls with penalty parameters [16]. This implementation uses a trust region on (11) and penalized virtual controls on (19) and (20).

The entire optimization problem is therefore:

$$\begin{aligned} \min \quad & \sum_{n=1}^{N} \Delta v_n \\ \text{s.t.} \quad & (11), (15), (19), (24) \quad n = 1, 2, \ldots, N \\ & (20), (23) \end{aligned} \tag{25}$$

The SCP process repeatedly solves (25) using a convex optimizer and updates the linearized constraints (11), (15) and (20) with the optimal solution from the previous iteration. The convergence of the algorithm is determined by the accuracy of the linearization when compared to truth.

In terms of implementation, `JuMP.jl` [17] was used to create and modify the convex problems and MOSEK to solve them.

We demonstrate this SCP approach by computing transfers from a particular $e = e_{lim}, \omega$ state to potential e, ω states, assuming a constant semi-major axis, inclination, and RAAN. Fig. 8 shows the Δv required, the resulting propagation time t_f, and the ratio $t_f/\Delta v$. We can see that translation distance $\Delta e\omega$ acts as a proxy for the required Δv.

IV. Results

Four different results are presented. The first two consider the $e - \omega$ translation strategy discussed in this paper, with $\lambda = 0$ to maximise the time between SK manoeuvres, and $\lambda = 1$ to balance time and translation distance. Two other strategies are also presented for completeness: *circularisation* and *convex-only*. The *circularisation* takes a similar approach to the $e - \omega$ translation strategy, applying manoeuvres only when the altitude violation occurs. However, instead of targeting a (e_0, ω_0) pair to maximise the subsequent ballistic segment, it circularises the orbit by targeting $e_0 = 0, \omega_0 = 0$. This should represent the upper bound for the $e-\omega$ strategy. In the *convex-only* strategy, the 90 day SK interval is discretised into 120 minute segments, with manoeuvres allowed at each segment. The only constraint is to maintain the altitude within 18 ± 9 km. This should provide a lower bound on $e - \omega$ strategy and an indication as to what the optimal Δv might be to maintain such an eLLO.

Table I and II show the results for 9×9 and 51×51 dynamics respectively. The station-keeping strategy was performed for a 90-day period starting from 21^{st} March 2024 at 12pm UTC, although this strategy is independent of the specific epoch used. Two different initial conditions were considered, both as a result of the grid search on i and ϕ shown in Figs. 7 and 6: the minimum number of manoeuvres and the minimum total translation distance accumulation. The first thing to note is the decrease in required Δv for the 51×51

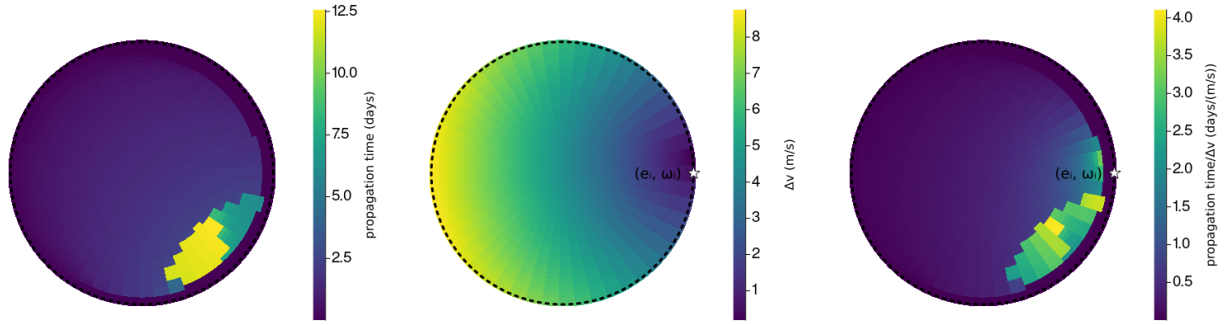

(a) Propagation time t_f before $e \geq e_{lim}$ (b) Δv for e, ω translation (c) Ratio $t_f/\Delta v$

Fig. 8: Example set of SCP transfers from a given $e = e_{lim}, \omega$ state to potential e, ω states, assuming a constant semi-major axis, inclination and RAAN. The Δv required, the resulting propagation time t_f, and the ratio $t_f/\Delta v$ are shown. We can see that translation distance $\Delta e\omega$ acts as a proxy for the required Δv. This is done with 9x9 spherical harmonics.

model compared to the 9×9 model, which demonstrates whilst the station-keeping strategy works for both, accurate estimates are best obtained at the desired model resolution, as higher-order spherical harmonics can, in some instances, be beneficial to orbit maintenance.

Figure 10 shows the results for the minimum manoeuvre initial condition. The subplots on the left show the altitude (blue) above the Moon's mean radius, 1737.4km, along with the perilune and apolune (red). The black markers along the x-axis indicate the periods where a manoeuvre was conducted within a 24-hour sliding window. This is similarly indicated in the *Coast (%)* column in the tables, although a 3 hour sliding window is used there. The right-hand subplots show an averaged evolution of e and ω throughout the 90-day period, where darker colours indicate earlier times.

The convex-only approach achieves a minimum Δv of 51.32 m/s for the minimum cumulative translation distance initial condition, indicating the translation distance acts as an appropriate proxy for the total Δv. However, this is not appropriate for an operational strategy due to the very high manoeuvre frequency (28.87% of the total time is within 3 hours of a manoeuvre) and the need to optimise the entire 90-day sequence together. However, the proposed $e-\omega$ strategy is able to achieve a minimum Δv of 75.86 m/s using the $\lambda = 1$ in the objective function. In this fashion, only the current manoeuvre to the target (e_0, ω_0) needs to be optimised, making it suitable as an onboard station-keeping strategy. This slightly outperforms the $\lambda = 0$ strategy in terms of Δv, it uses slightly more manoeuvres (7.37% of the total time is within 3 hours of a manoeuvre as opposed to 5.59%). It is clear that optimising the target (e_0, ω_0) significantly increases the performance, both in terms of Δv and frequency of manoeuvres, compared to the circularisation strategy, which for the equivalent initial condition is 1.95x more expensive.

If the objective is to minimise the number of manoeuvres, then other initial condition can be used, where the $e - \omega$ strategy maximising the time between manoeuvres ($\lambda = 0$) reduces total time within 3 hours of a manoeuvre to 5.23%, 12 total station keeping sequences. This also only requires 77.23 m/s Δv, and offers long coast arcs between manoeuvres, an attractive option from the perspective of operational costs.

V. Conclusion

This paper presents a station-keeping strategy for extremely low-altitude lunar orbits (eLLOs) using eccentricity-vector control. The desired altitude range of 18 ± 9km is too low for potentially stable frozen orbits, however, the low eccentricity results in an $e - \omega$ profile that exhibits an almost repetitive pattern. This "translation theorem" enables a station-keeping strategy that can control the eccentricity vector by optimising the initial conditions in the $e - \omega$ phase space using a single propagation. A grid search is used to find the inclination and body-fixed argument of ascending node that minimise the total number of manoeuvres or minimises the total cumulative translation distance throughout a 90-day station-keeping period. Then, sequential convex programming (SCP) is used to optimise the manoeuvres to provide a guidance strategy that could be implemented onboard. The results indicate a minimum of 12 station-keeping sequences, using a total of 77.23 m/s can maintain this eLLO. This can be reduced to 75.86 m/s at the cost of slightly increasing the number of manoeuvres required. The station-keeping strategy can be readily applied to different altitude lunar orbits, with varying altitude constraints.

Acknowledgements

Harry Holt is currently funded through the generous financial support from the Warwick & Judy Smith Engineering Endowment Fund and the support of the University of Auckland Foundation and Faculty of Engineering.

References

[1] A. S. Konopliv, W. Sjogren, R. Wimberly, R. Cook, and A. Vijayaraghavan, "A high-resolution lunar gravity field and predicted orbit behavior," in *AAS/AIAA Astrodynamics Specialist Conference*, pp. 16–19, Aug. 1993.

[2] M. Lara, "Design of long-lifetime lunar orbits: A hybrid approach," *Acta Astronautica*, vol. 69, pp. 186–199, Aug. 2011.

[3] R. P. Russell and M. Lara, "Long-Lifetime Lunar Repeat Ground Track Orbits," *Journal of Guidance, Control, and Dynamics*, vol. 30, pp. 982–993, July 2007.

TABLE I: Comparison of SK strategies for different initial conditions with 9x9 Spherical Harmonics.

Initial Conditions	i_0	ϕ_0	Approach	Altitude Range (km)	Coast (%)	ΔV (m/s)
Minimum Manoeuvres	86	357.76	$e-\omega\ \lambda=0$	8.98-27.01	92.63	91.78
			$e-\omega\ \lambda=1$	8.99-27.01	91.15	88.46
			Circularisation	8.99-27.02	83.97	165.20
			Convex-only	8.92-27.09	67.54	67.29
Minimum Cumulative Translation	94	177.76	$e-\omega\ \lambda=0$	8.98-27.01	91.77	91.12
			$e-\omega\ \lambda=1$	8.98-27.01	90.93	88.84
			Circularisation	8.97-27.02	86.50	135.62
			Convex-only	8.92-27.10	66.70	65.47

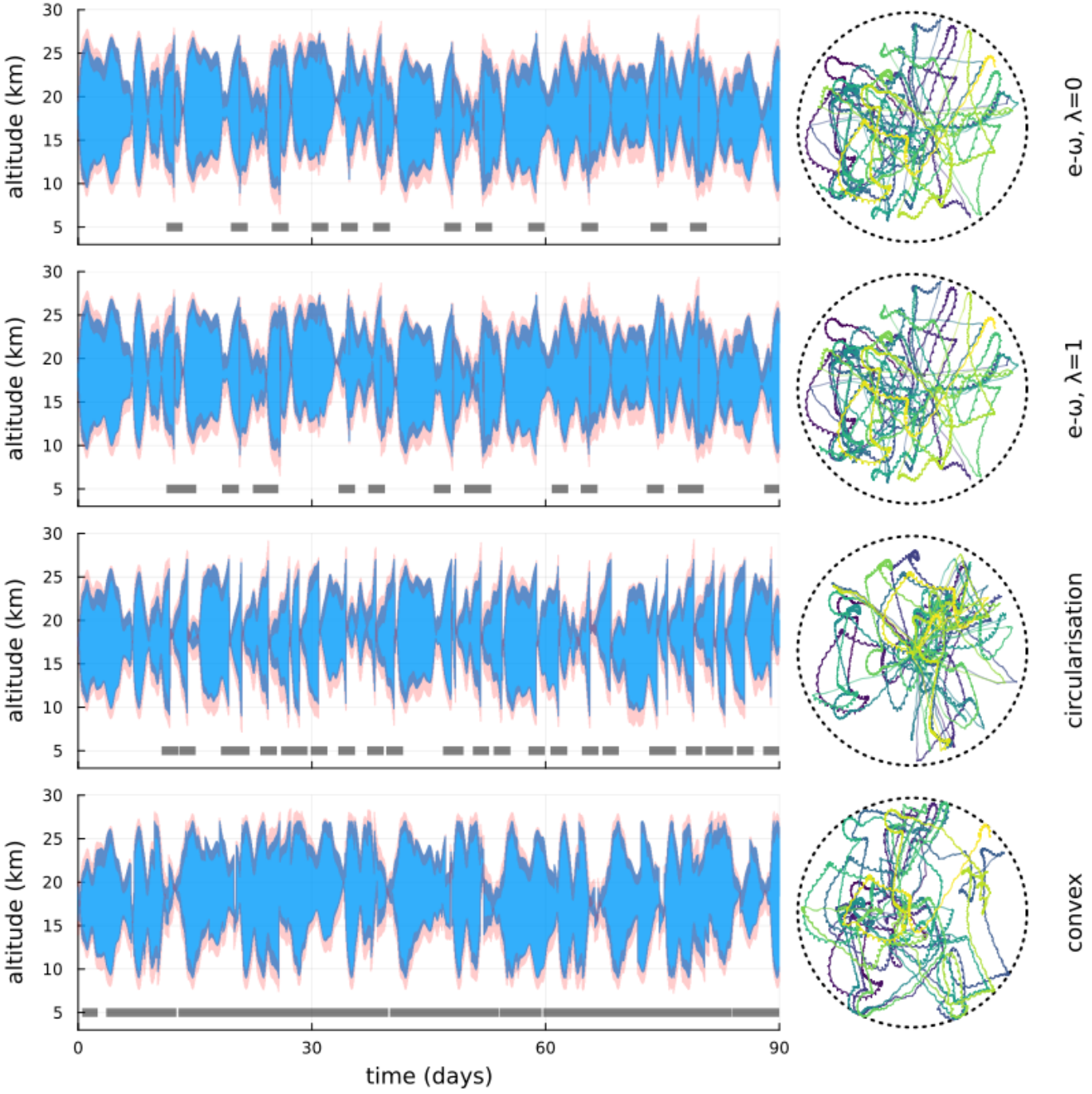

Fig. 9: Comparison of SK strategies for different initial conditions with 51x51 Spherical Harmonics, using the Minimum Manoeuvres initial condition of $i_0 = 88°$ and $\phi_0 = 342.76°$.

TABLE II: Comparison of SK strategies for different initial conditions with 51x51 Spherical Harmonics.

Initial Conditions	i_0	ϕ_0	Approach	Altitude Range (km)	Coast (%)	ΔV (m/s)
Minimum Manoeuvres	88	342.76	$e-\omega$ $\lambda=0$	9.00-27.00	94.77	77.23
			$e-\omega$ $\lambda=1$	9.00-27.00	93.16	81.11
			Circularisation	9.00-27.00	89.23	124.74
			Convex-only	8.98-27.02	71.71	54.44
Minimum Cumulative Translation	87	7.76	$e-\omega$ $\lambda=0$	9.00-27.00	94.41	76.91
			$e-\omega$ $\lambda=1$	9.00-27.00	92.63	75.86
			Circularisation	9.00-27.00	86.17	148.03
			Convex-only	8.86-27.15	71.13	51.32

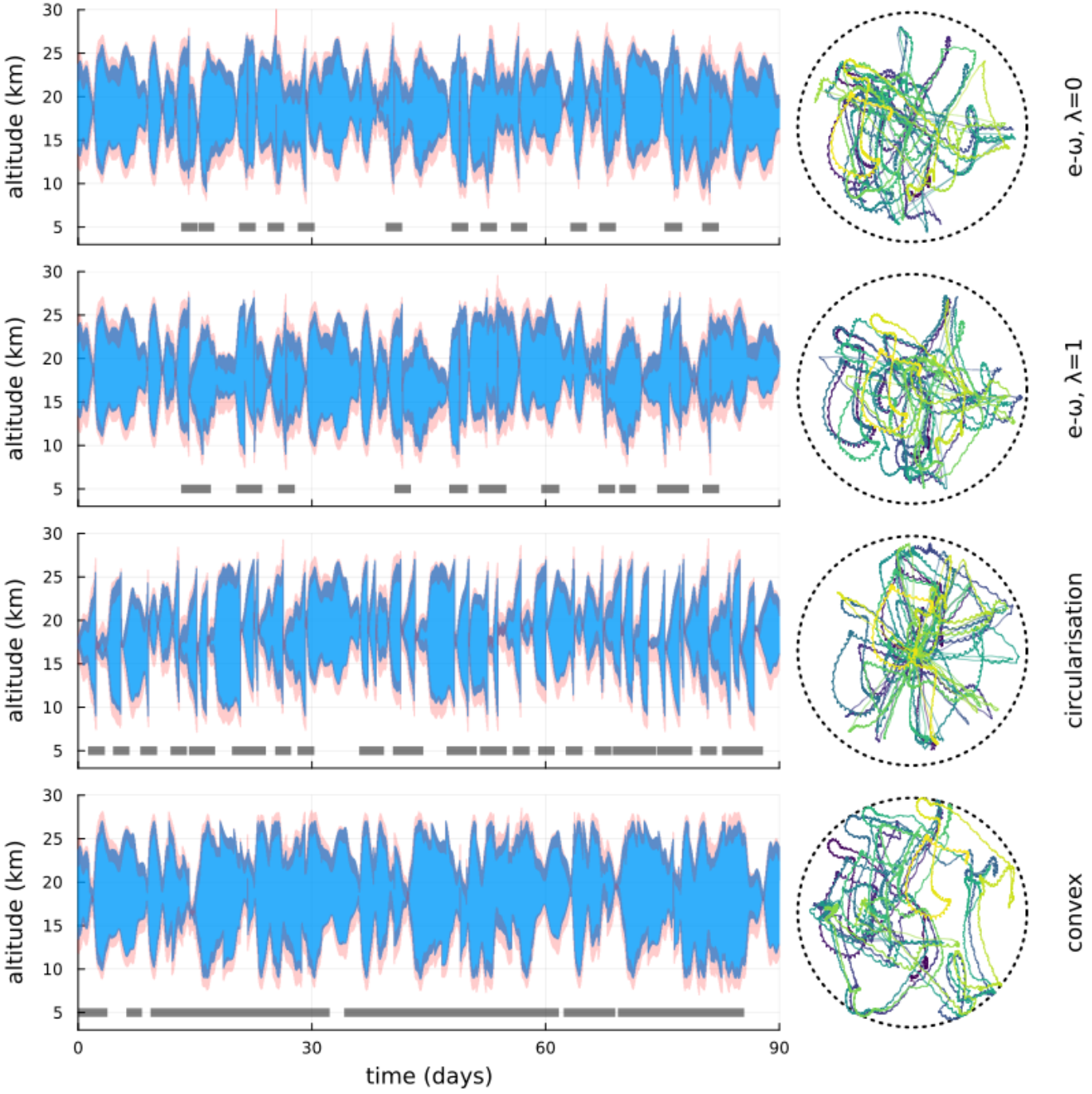

Fig. 10: Comparison of SK strategies for different initial conditions with 51x51 Spherical Harmonics, using the Minimum Cumulative Translation initial condition of $i_0 = 87°$ and $\phi_0 = 7.76°$.

[4] D. Folta and D. Quinn, "Lunar frozen orbits," in *AIAA/AAS astrodynamics specialist conference and exhibit*, Aug. 2006. tex.eprint: https://arc.aiaa.org/doi/pdf/10.2514/6.2006-6749.

[5] M. Beckman and R. Lamb, "Stationkeeping for the Lunar Reconnaissance Orbiter (LRO)," in *20th International Symposium on Space Flight Dynamics*, Sept. 2007.

[6] S. K. Singh, R. Woollands, E. Taheri, and J. Junkins, "Feasibility of quasi-frozen, near-polar and extremely low-altitude lunar orbits," *Acta Astronautica*, vol. 166, pp. 450–468, Jan. 2020.

[7] S. Buchan, F. Downey, B. Hartig, D. Busan, J. Cook, C. Tay, T. Ward, R. Howie, P. Bland, and J. Paxman, "Binar Space Program: Mission Two Payloads and Operations Plan," in *AIAA/USU Conference on Small Satellites, Next on the Pad, SSC22-WKVIII-07*, Aug. 2022.

[8] F. Downey, S. Buchan, B. Hartig, D. Busan, J. Cook, R. Howie, and P. Bland, "Binar Space Program: Binar-1 Results and Lessons Learned," in *AIAA/USU Conference on Small Satellites, Recent Launches - Research & Academia, SSC22-WKII-06*, Aug. 2022.

[9] P. Bland, "Binar Prospector: An Australian Lunar Resource Prospecting Mission," in *Lunar Surface Science Workshop 17: Defining a Coordinated Lunar Resource Evaluation Campaign*, July 2022.

[10] W. M. Kaula, *Theory of satellite geodesy. Applications of satellites to geodesy*. Waltham, Massachusetts: Blaisdell, 1966. Reprint: Dover, Mineola, New York, 2000.

[11] M. Lara, *Hamiltonian Perturbation Solutions for Spacecraft Orbit Prediction. The method of Lie Transforms*, vol. 54 of *De Gruyter Studies in Mathematical Physics*. Berlin/Boston: De Gruyter, 1 ed., 2021. Erratum: [link].

[12] D. Malyuta, T. P. Reynolds, M. Szmuk, T. Lew, R. Bonalli, M. Pavone, and B. Açıkmeşe, "Convex Optimization for Trajectory Generation: A Tutorial on Generating Dynamically Feasible Trajectories Reliably and Efficiently," *IEEE Control Systems*, vol. 42, pp. 40–113, Oct. 2022.

[13] J. H. Verner, "Numerically optimal Runge–Kutta pairs with interpolants," *Numerical Algorithms*, vol. 53, pp. 383–396, Mar. 2010.

[14] C. Rackauckas and Q. Nie, "DifferentialEquations.jl – A Performant and Feature-Rich Ecosystem for Solving Differential Equations in Julia," *Journal of Open Research Software*, vol. 5, p. 15, May 2017.

[15] J. Revels, M. Lubin, and T. Papamarkou, "Forward-Mode Automatic Differentiation in Julia," Apr. 2016.

[16] C. Hofmann, *Computational Guidance for Low-Thrust Spacecraft in Deep Space Based on Convex Optimization*. PhD thesis, Politecnico di Milano, 2023.

[17] M. Lubin, O. Dowson, J. D. Garcia, J. Huchette, B. Legat, and J. P. Vielma, "JuMP 1.0: Recent improvements to a modeling language for mathematical optimization," *Mathematical Programming Computation*, vol. 15, pp. 581–589, Sept. 2023.